Solid Earth Discuss., 4, 1025–1067, 2012
www.solid-earth-discuss.net/4/1025/2012/
doi:10.5194/sed-4-1025-2012

Solid Earth Discussions

Reprocessed height time series of GPS stations at tide gauges

S. Rudenko[1], N. Schön[1,2], M. Uhlemann[1], and G. Gendt[1]

[1]Helmholtz Centre Potsdam GFZ German Research Centre for Geosciences, Telegrafenberg, 14473 Potsdam, Germany
[2]Bristol Glaciology Centre, School of Geographical Sciences, University of Bristol, University Road, Bristol BS8 1SS, UK

Received: 21 June 2012 – Accepted: 27 June 2012 – Published: 26 July 2012

Correspondence to: S. Rudenko (rudenko@gfz-potsdam.de) and N. Schön (nana.schoen@bristol.ac.uk)

Published by Copernicus Publications on behalf of the European Geosciences Union.

Abstract

Precise weekly positions of 403 Global Positioning System (GPS) stations located worldwide are obtained by reprocessing GPS data of these stations at the time span from 4 January 1998 until 29 December 2007. The used processing algorithm and models as well as the solution and results obtained are presented. Vertical velocities of GPS stations having tracking history longer than 2.5 yr are computed and compared with the estimates from the colocated tide gauges and other GPS solutions. Examples of typical behavior of station height changes are given and interpreted. The derived time series and vertical motions of continuous GPS at tide gauges stations can be used for correcting tide gauge estimates of regional and global sea level changes.

1 Introduction

Satellite radar altimetry and tide gauge measurements are the primary methods for sea level change investigations. The former one measures absolute sea level during last 35 yr using data from altimetry satellite missions GEOS3, SEASAT, GEOSAT, ERS-1, ERS-2, GFO, TOPEX/Poseidon, Jason-1, Envisat, Jason-2, Cryosat-2 and recently HY-2A. Over 1750 tide gauge stations located worldwide measure relative sea level providing long time series (totally longer than 120 yr). Therefore, analysis of tide gauge measurements with the purpose of long-term sea level change research requires a well defined reference frame. Such reference frame can be realized through precise positions of GPS stations located at or near tide gauges which is one of the purposes of the GPS Tide Gauge Benchmark Monitoring Pilot Project (TIGA) (Schöne et al., 2009) of the International Global Navigation Satellite System (GNSS) Service (IGS). The required accuracies are about 5–10 mm for station positions and less than 1 mm yr^{-1} for vertical motions. Such solutions were derived by different reserch groups in 2002–2006 (e.g. Zhang et al., 2008) using relative models for antenna phase centre variations (PCV) and older processing models. However, switch within the IGS from

SED
4, 1025–1067, 2012

using a relative to an absolute PCV model mainly affecting the station height, use of new processing software, models and strategies, inclusion of new TIGA GPS stations in the solutions required and made possible a reprocessing within the TIGA project.

Different authors used GPS measurements to investigate crustal motions at tide gauges and sea level changes regionally (e.g. Buble et al., 2010; Sanchez et al., 2009) and globally (e.g. Wöppelmann et al., 2009). King and Watson (King et al., 2010) recently showed the influence of multipath and geometry effects on the long GPS coordinate time series.

The quality assessment of the recently reprocessed GPS realization of the terrestrial reference frame (Collilieux et al., 2011) shows that the GPS-derived origin is at the centimeter level consistent with the Satellite Laser Ranging (SLR) one with a drift lower than 1 mm yr^{-1}. Bouin and Wöppelmann (Bouin and Wöppelmann, 2010) found agreement within 2 mm yr^{-1} of tide gauge estimates and vertical velocities for 84 % of the GPS stations colocated with tide gauges by analyzing 10 yr of continuous GPS data of more than 200 permanent GPS stations distributed worldwide. Global sea-level rise estimates calculated from tide gauge records corrected using GPS data depend on the terrestrial reference frame used. Thus, errors in the reference frame scale rate influence the estimated global sea level rise (Collilieux and Wöppelmann, 2011).

In this paper, we describe the procedure, models used and the results obtained from the analysis of continuous GPS data from a global network of 403 GPS stations at about 10 yr time span (1998–2007). 187 stations are located at or near tide gauges. Absolute PCV and other up-to-date models are used. ITRF2005 (Altamimi et al., 2007) was used as a priori terrestrial reference frame. Vertical velocities of GPS stations with time series longer than 2.5 yr are computed. We compare our solution with the estimates from colocated tide gauges as well as with the GPS-derived vertical velocities from GFZ previous and an external solutions.

The remainder of the paper is organized in the following way. The GPS data processing algorithm and the input data, reference frames and models used are described in Sect. 2. The main results of GPS data reprocessing are given in Sect. 3.

SED
4, 1025–1067, 2012

The methodology of station vertical velocity computation and some examples of station height changes are given in Sect. 4. Finally, the obtained results are discussed (Sect. 5), conclusions are drawn and outlook is given.

2 GPS data processing algorithm

GPS data of the global network of 403 stations covering time span 4 January 1998–29 December 2007 (GPS weeks 939 to 1459) were analysed using EPOS-Potsdam software (version 7) (Gendt et al., 1994) recently elaborated. The network includes 187 continuous GPS at tide gauges (TIGA) stations and 216 IGS stations. The network was split in two subnetworks of up to 216 globally stations each. The subnetworks are combined to form daily solutions using up to 30 distributed worldwide IGS05 reference stations in the ITRF2005 datum (cluster connectors). A global map of the station network used for reprocessing is given in Fig. 1. The subnetwork of IGS stations was used to estimate GPS satellite orbits, clocks and Earth rotation parameters that were needed for processing GPS data of the TIGA station subnetwork. Daily solutions are combined into three-day solutions by applying orbit continuity constraints (Beutler et al., 1996).

The observation data, reference frames, measurement models and orbit models used are described in Table 1. Terrestrial reference frame was defined in the following way. Initial coordinates of stations present in ITRF2005 (Altamimi et al., 2007) were taken from ITRF2005 and estimated for remaining stations. Initial values of station velocities were used from ITRF2005, if available, and computed using NNR-NUVEL1A model (McCarthy et al., 2003) for the rest stations.

GPS data from a few hundred stations were processed using data processing strategy for huge GNSS global networks (Ge et al., 2006). The following parameters are estimated in the least-square adjustment. The X, Y, Z station coordinates of all stations are estimated weekly using free network strategy with constraints 1–1000 m to a priori values, no station is fixed. Receiver and satellite clocks are solved for at each epoch assuming white noise process. One receiver clock is fixed and used as a time

SED
4, 1025–1067, 2012

reference. Satellite initial position and velocity, solar radiation pressure scale, y-bias, sine/cosine terms and stochastic impulses (at noon) are estimated for all satellites once per arc. Yaw rate is adjusted for BLOCK II/IIA satellites during shadow crossing. Troposphere zenith delay coefficients are solved for each station at 1 h intervals. Troposphere gradients in elevation and azimuth are estimated every 12 h for each station. Ambiguities are fixed according to (Ge et al., 2005). The x and y Earth pole coordinates and their rates, Length-of-day and GPS satellite phase center offsets are adjusted daily. In a weekly solution, UT1 is fixed for the first day and estimated for the remaining days.

3 Results of GPS data reprocessing

The GFZ TIGA GT1 solution contains weekly coordinates of GPS stations, daily values of the Earth rotation parameters and their rates as well as satellite antenna offsets and is available in the Solution (Software/technique) Independent Exchange (SINEX) format via anonymous ftp at TIGA archive ftp://ftp.gfz-potsdam.de/pub/transfer/kg_igs/igstiga/solutions/ as files /wWWWW/gftWWWW7.snx.Z and at CDDIS ftp://cddis.gsfc.nasa.gov/gps/products/WWWW/repro1/ as files gt1WWWW7.snx.Z, where WWWW stands for GPS week in the range from 0939 till 1459.

The number of stations included in the weekly solutions reaches within the time interval up to 300 as it can be seen from Fig. 2, which shows also the rapidly growing observation network in the first years.

As an indicator of relative solution stability the coordinate repeatabilities of daily solutions with respect to the weekly solution were calculated. The averaged values per week over all stations are given in Fig. 3. It is clearly visible that after Anti Spoofing (AS) was switched of for GPS in May 2005 the North and East coordinate solutions get more stable and reach even a level of 1 mm and for the Up component 3 mm in 2007. These effects are also linked to enhancements in used station eqiupment.

For an absolute assessment of the coordinate solutions a 7-parameters transformation was done with respect to the IGS combined solution of Repro1 (Dow et al., 2009).

SED
4, 1025–1067, 2012

The standard deviation of solution residuals weighted average is shown in Fig. 4. The accuracy of North and East components is for the investigated time span of about 1 mm and the Up component reaches about 3 mm at the end. Based on these results it can be stated that the required position accuracies are fullfiled needed for determinantion of accurate station height time series and that a precise reference frame was realized.

The daily adjusted values of x and y Earth pole coordinates and Lenght-of-day (LOD) are compared to the combined solution of the first IGS Reprocessing campaign (IG1). The good agreement between the two solutions in x and y pole coordinates with mean and standard deviation of -0.012 ± 0.056 and -0.026 ± 0.049 mas and LOD with $0.00 \pm 0.023\,\mathrm{ms\,d^{-1}}$ can be seen from Fig. 5.

4 Station height changes

4.1 Methodology of the station vertical velocity computation

Vertical trends were determined from the GT1 SINEX files by extracting the vertical coordinates and converting them to longitude, latitude and height using the WGS84 geoid model. The time series were then fitted to extract a linear trend using the standard deviation values as reciprocal weights to account for measurement errors. Trend changes were determined using the BFAST package (Verbesselt et al., 2010). The number of breakpoints (minimum sequence length) was adjusted so as to obtain reasonable estimates of the trend changes, mirroring the assumed underlying processes.

Antenna changes and other events influencing the vertical trend component were taken from the GPS log files for the respective stations. Some of the GPS stations examined here are located at tide gauges. Here, the trends from the tide gauges were compared with the GPS trends and sea level radar altimetry data from the TOPEX mission to separate the origin of the trend signal where possible. TOPEX/Poseidon sea level anomaly data was provided by Saskia Esselborn, GFZ; a seasonal component was extracted using the Loess algorithm from the STL package (Cleveland et al., 1990).

SED
4, 1025–1067, 2012

No atmospheric corrections were applied to the GPS data, except for BRAZ station, where the hydrological seasonal cycle was the main point of interest, and both VAAS and MAR6 stations, for which also hydrological issues were reviewed.

While most stations show consistent, steady trends, a minority shows deviations caused by antenna or receiver changes. Following the recommendations by Blewitt and Lavallée (Blewitt et al., 2002), stations with time series shorter than 2.5 yr were not considered for trend estimation. Vertical velocities of GPS stations located at tide gauges and some IGS stations are given in Table 2.

The time series of height changes of all GPS stations of GT1 solution are available at ftp://ftp.gfz-potsdam.de/pub/home/ig/nana/GPS_station_heights/. In the following, a few interesting examples are treated in detail.

4.2 Stations with prominent secular height trend

4.2.1 Plate tectonics: Neah Bay NEAH, Canada

Neah Bay, Washington lies on the Juan de Fuca Strait in the Cascadia Subduction zone, which is subject to crustal uplift as the North American Plate is shifted over the Juan de Fuca Plate. The GPS time series shows a secular trend of $3.96 \pm 0.02\,\mathrm{mm\,yr^{-1}}$ ($4.0 \pm 0.0\,\mathrm{mm\,yr^{-1}}$ with a seasonal signal removed) (Fig. 6). This is in accordance with the results obtained by Verdonck (Verdonck, 2006), who arrives at a $4.0 \pm 0.1\,\mathrm{mm\,yr^{-1}}$ trend through the analysis of tide gauge data. Sea level from altimetry yields a trend of $4.0 \pm 0.9\,\mathrm{mm\,yr^{-1}}$, when a seasonal component is removed beforehand ($-4.3 \pm 1.5\,\mathrm{mm\,yr^{-1}}$ for the full data). This is consistent with the fact that the nearest TOPEX grid point lies on the North American Plate as well and is thus also subject to uplift in the region.

SED
4, 1025–1067, 2012

4.2.2 Glacial isostatic adjustment (Fennoscandia): Vaasa VAAS (Vaasa tide gauge), Mårtsbo MAR6, Sweden (Nedre Gavle tide gauge), and Skellefteå SKE0, Sweden (Furuogrund TG)

These three stations, all located around the Gulf of Bothnia, are subject to land movement processes due to glacial isostatic adjustment (GIA). All stations show large secular uplift rates with Skellefteå leading at $10.80 \pm 0.06\,\mathrm{mm\,yr^{-1}}$, followed by Vaasa at $8.66 \pm 0.04\,\mathrm{mm\,yr^{-1}}$ and Mårtsbo ($7.62 \pm 0.01\,\mathrm{mm\,yr^{-1}}$).

The Skellefteå CGPS station lies in the vicinity of Furuogrund tide gauge (approximately 11 km distance). The tide gauge trend yields $10.2 \pm 0.3\,\mathrm{mm\,yr^{-1}}$. With the seasonal signal removed, the trend reaches $15.9 \pm 0.2\,\mathrm{mm\,yr^{-1}}$. The TOPEX trend (1994–2001) of the nearest grid point (64° N 22° E) lies at $6.4 \pm 2.2\,\mathrm{mm\,yr^{-1}}$. Theoretically, the GPS-derived land movement trend and TOPEX altimeter data derived trend should add up to the trend from the tide gauge data. The differences can be explained by geoid variations caused by GIA, which will be measured by the TOPEX radar altimeter, but not by GPS. It should also be kept in mind that an atmospheric pressure correction was applied to the TOPEX altimeter data, but not to the GPS and tide gauge data.

Nedre Gavle, located at approximately 10 km distance from the MAR6 GPS station, has a trend of $6.0 \pm 0.2\,\mathrm{mm\,yr^{-1}}$ (1896–1986). Since the gauge stopped operating in 1986, there is no common period with the GPS station. However, the accordance with the land movement trend at Mårtsbo ($7.62 \pm 0.01\,\mathrm{mm\,yr^{-1}}$) is satisfactory. The next nearest TOPEX grid point (61° N 18° E) shows a trend of $4.0 \pm 2.5\,\mathrm{mm\,yr^{-1}}$ (1994–2001).

Despite their distance (>340 km), the GPS time series for Vaasa and Mårtsbo are strongly correlated at $R^2 = 0.93$ (Fig. 7). When reduced for atmospheric loading, the correlation drops only marginally to $R^2 = 0.92$. A large part of this is due to the trend, however, even the de-trended time series score a $R^2 = 0.45$ correlation. Deviations between the two series consist mainly in an annual multi-week drift at Vaasa, which is caused by snow cover on the antenna. Figure 8 shows that the drift signals coincide

SED
4, 1025–1067, 2012

with the periods of increased snow coverage in the area. The snow cover data was taken from Robert Dill's LSDM hydrology model (Dill, 2008). Its influence on the correlation is checked by decomposing the de-trended time series and determining the correlations for the respective components. When the linear trend is removed, the time series correlate at $R^2 = 0.73$ for the residual nonlinear trend, and $R^2 = 0.59$ for the remainder. Only the snow-dominated seasonal cycle shows no correlation at $R^2 = -0.09$. It is worth a remark that the snow disturbance is correctly removed by the STL algorithm when removing the seasonal cycle. This example shows that hydrological errors occurring at a seasonal frequency can be easily and automatically removed when the seasonal cycle is calculated by taking the multi-year monthly mean, instead of fitting a sine. The tide gauges show the same strong correlation, with $R^2 = 0.95$ for the full time series and $R^2 = 0.91$ for the de-trended time series, in both cases for the common period (1896–1986).

4.2.3 Glacial isostatic adjustment (Canada): Churchill CHUR and Kuujjuarapik KUUJ, Canada

Both Churchill and Kuujjuarapik lie in the Hudson bay, which is also subject to glacial isostatic adjustment. Both stations show strong secular uplift trends: $9.67 \pm 0.03\,\mathrm{mm\,yr^{-1}}$ (CHUR) and $11.52 \pm 0.06\,\mathrm{mm\,yr^{-1}}$ (KUUJ). The two time series show strong correlation for both seasonal ($R = 0.85$) and trend component ($R = 1.00$) (Fig. 9). The tide gauge at Churchill yields a trend of $7.2 \pm 1.1\,\mathrm{mm\,yr^{-1}}$ for the 1998–2007 period. For the full time series (1940–2009) the trend is even higher at $13.6 \pm 0.1\,\mathrm{mm\,yr^{-1}}$, with a seasonal component removed beforehand ($11.2 \pm 0.2\,\mathrm{mm\,yr^{-1}}$ for the full data).

4.2.4 Bogota BOGT, Colombia

This station is a peculiar example. Located on the top of the IGAC Building in Bogotá, which, possibly, due to construction faults, has been continuously subsiding

SED
4, 1025–1067, 2012

during the past years. This station was treated in (Kaniuth et al., 2001). The vertical trend has more than doubled since 2001, now reaching the alarming rate of $-44.21 \pm 0.19\,\mathrm{mm\,yr^{-1}}$ (Fig. 13).

4.3 Stations with trend changes

4.3.1 Trend changes in GPS stations: Arequipa AREQ, Peru

Arequipa lies in Southwestern Peru, in the subduction zone where the oceanic Nazca plate is subducted under the South American plate along the Peru-Chile trench. It is an interesting example of a trend change, as the station recorded the 2001 Arequipa-Camana-Tacna area (M:8.4W) earthquake (CDEW, 1990) and its effects on land movement. The trend change is visible in the time series from GPS week 1120 (25 June 2001), two days after the date of the earthquake on 23 June 2001 (Fig. 12). Before the event, the trend was $-2.6 \pm 0.5\,\mathrm{mm\,yr^{-1}}$, changing direction to a positive $4.2 \pm 0.1\,\mathrm{mm\,yr^{-1}}$ uplift trend afterwards. From 2005 on, a slight reduction of the trend can be observed, but a connection with a seismic event could not be established.

4.3.2 Trend change in tide gauge data: Kushimoto P208, Japan

Kushimoto (GPS station P208) is located at the southern tip of the Kii Peninsula, Wakayama prefecture. It is situated within the Nankai trough subduction zone and was affected, among others, by the 1946 Nankai earthquake (M = 8) (CDEW, 1990). Sato mentions, that prior to the 1944 earthquake, the southern part of the peninsula is supposed to have subsided with a constant rate of 5–6 $\mathrm{mm\,yr^{-1}}$. The tide gauge record shows a clear trend change coinciding with the minor (M = 5.6) Wakayama prefecture earthquake of 9 May 1987 (CDEW, 1990). The land movement trend from the tide gauge before the earthquake is a moderate $-0.6 \pm 0.2\,\mathrm{mm\,yr^{-1}}$, increasing by more than 800 % to $-6.5 \pm 0.2\,\mathrm{mm\,yr^{-1}}$ after the earthquake. The vertical land movement trend determined from the P208 permanent GPS station over the 2005–2010 period

SED
4, 1025–1067, 2012

is $-6.3 \pm 0.1\,\mathrm{mm\,yr^{-1}}$. A comparison with the TOPEX (1994–2001) sea level anomaly trend ($-1.8 \pm 1.7\,\mathrm{mm\,yr^{-1}}$) strengthens the assumption that the major part of the tide gauge trend is caused by the land movement (Fig. 14).

Apparently, after the 1987 earthquake, the southern part of the Kii peninsula has taken up its original subsiding motion. Still, Isoda (Isoda et al., 2004) remarked that the Kushimoto tide gauge is located on the (uplifting) Eurasia plate. Emery and Aubrey (Emery et al., 1991) mention submergence caused by groundwater extraction as another possible cause for subsidence.

4.3.3 Trend change in tide gauge data and GPS data: Aburatsu, Japan

Another example of a trend change is Aburatsu, located at Nichinan, Miyazaki prefecture, Japan. One trend change occurs in the aftermath of the July, 1970 Miyazaki prefecture earthquake (M = 6.7). Another trend change in April 1984 coincides with the Kagoshima prefecture earthquake of 28 April 1986 (M = 4.4) (CDEW, 1990).

An analysis of the GPS time series shows a trend change from GPS week 1342 (26 September 2005). Before this (May 2003–May 2005), the land movement trend from the GPS time series, $-3.3 \pm 0.6\,\mathrm{mm\,yr^{-1}}$, explains a large part of the sea level rise trend of $3.5 \pm 1.0\,\mathrm{mm\,yr^{-1}}$ for the time after the last trend change (from April 1987). After the 2005 trend change, the land movement switches sign to $2.1 \pm 0.7\,\mathrm{mm\,yr^{-1}}$. Drops in the time series as depicted in Fig. 11 clearly mark the impact of the the Oita 2006 (12 June, M = 6.2) and 2007 (6 June, M = 4.9) earthquakes. The impact of the 2005 Fukuoka earthquakes (CDEW, 1990) (20 and 22 March, 20 April, and 5 May) is less clear, but the trend change begins a few weeks after the earthquake.

4.3.4 Variations caused by hydrological processes: BRAZ, Brasilia, Brasil

The time series of this station, located in the Roncador Ecological Reserve, approximately 35 km south of Brasilia, exhibits strong annual variations from hydrological effects. In (van Dam, 2001), van Dam and co-authors already mention BRAZ as an

SED
4, 1025–1067, 2012

example for strong annual variations due to hydrological water loading, although, at the time of publication there was only a short time series available.

To separate the atmospheric pressure loading effects from the hydrological variations, a pressure correction was applied following (van Dam et al., 1994). NCEP 6-hourly surface pressure data were convolved with Farrell's Greens functions using the programme provided on Tonie van Dam's web site (van Dam, 2010). This technique is outlined in (van Dam et al., 1994).

From 2006 on, a strong negative trend is visible in the GPS time series. This decrease can be found in GRACE data (Kurtenbach et al., 2009). For the comparison, the GRACE data were re-sampled to monthly values and filtered, then converted to equivalent water height. The gridded product was provided by Henryk Dobslaw, GFZ. For a qualitative comparison, the data is scaled by factor 150 in Fig. 10. The comparison with water mass data from the Land Surface Discharge Model (LSDM) (Dill, 2008) also shows a strong decrease in water column height. The cause of the subsidence is apparently the drought that hit region in late summer and fall of 2007 (EM-DAT, 2011).

4.4 Stations with zero height trend

Tuktoyaktuk (TUKT) station in Northwestern Canada is an example for a site with a height trend very close to zero ($-0.01 \pm 0.02\,\mathrm{mm\,yr^{-1}}$). Located close to the Alaskan border, the station is apparently neither affected by the positive GIA signal centered on Eastern Canada, nor by the land movement signals caused by recent ice loss (Larsen et al., 2004) commonly found in South Alaska. The moderate length of the time series (4.3 yr) however, makes this assessment a preliminary one. The seasonal cycle produces a spurious trend ($0.5 \pm 0.3\,\mathrm{mm\,yr^{-1}}$) if not removed (Fig. 15).

SED
4, 1025–1067, 2012

5 Discussion

The linear height trends obtained in this work have been compared with previous solutions. Thus, our solution (Table 2) contains linear trends additionally for the following 38 GPS stations not present in the previous GFZ solution (Zhang et al., 2008): 0194, ANDE, ANDO, ANTA, BUR1, CSAR, NCDK, NEIA, P102, P103, P104, P108, P109, P110, P112, P114, P115, P116, P117, P118, P119, P120, P124, P201, P202, P203, P204, P206, P209, P211, P212, P213, PAPE, PLUZ, REYZ, SKE0, TUKT, VTIS, WLAD due to the inclusion of GPS data from these stations located in Brazil, Canada, Iceland, Israel, Japan, Norway, Poland, Spain, Sweden, Tasmania, Turkey, the USA and on Tahiti in the GT1 solution. This is a notable contribution to the densification of the network of GPS stations processed.

The vertical velocities of our solution show for the most stations much better agreement (within 1 mm yr^{-1} and less) with the recent solution of Universite de La Rochelle (Bouin and Wöppelmann, 2010) (both use IGS absolute phase centre corrections for both tracking and transmitting antennas and more recent models) than with the previous GFZ solution (Zhang et al., 2008) utilises relative phase centre corrections and some older models (Table 3).

6 Conclusions

We have reprocessed GPS data from the global network of 403 GPS stations at 10 yr time span (1998–2007) using new models and algorithms and derived time series of weekly coordinates of these stations. The station coordinate repeatabilities of daily solutions with respect to the weekly ones reach 1 mm in the North and East components and 3 mm in the Up one. Vertical velocities of GPS stations having tracking history longer than 2.5 yr were computed and compared with the estimates from tige gauge data and some other GPS-derived solutions. Some examples of different types of station vertical velocities are presented. The comparion of the vertical velocities of

SED
4, 1025–1067, 2012

GPS stations of our solution with some other solutions including the recent solution of Universite de La Rochelle indicate that the accuracy of vertical velocities is below 1 mm yr^{-1} for the most GPS stations of our solution. The time series of heights of GPS stations colocated at tide gauges and vertical velocities at these stations can be used to correct the estimates of regional and global sea level changes based on tide gauge data. It is planned to perform a new reprocessing of continuos GPS data at longer time span (1994–2011) for an increased number of GPS stations at tide gauges by using newer models and ITRF2008 as a priori terrestrial reference frame within IGS second data reprocessing campaign. This will allow to compute a longer time series of station coordinates for a larger number of GPS stations with an increased accuracy of vertical velocity.

Acknowledgements. The authors thank T. Schöne (GFZ) for useful discussions. GPS data available from IGS, TIGA and some other stations and agencies were used in this study. The research was supported by German Ministry of Education and Research (BMBF) within the GEOTECHNOLOGIEN geoscientific *R&D* programme (SEAVAR Project). The study described in Sect. 4 was performed by N. Schön.

References

Altamimi, Z., Collilieux, X., Legrand, J., Garayt, B., and Boucher, C.: ITRF2005: A new release of the International Terrestrial Reference Frame based on time series of station positions and Earth Orientation Parameters, J. Geophys. Res., 112, B09401, doi:10.1029/2007JB004949, 2007. 1027, 1028, 1042

Bar-Sever, Y. E.: A new model for GPS yaw attitude, J. Geodesy, 70, 714–723, doi:10.1007/BF00867149, 1996. 1042

Beutler, G., Brockmann, E., Hugentobler, U., Mervart, L., Rothacher, M., and Weber, R.: Combining consecutive short arcs into long arcs for precise and efficient GPS orbit determination, J. Geodesy, 70, 287–299, doi:10.1007/s001900050019, 1996. 1028

Blewitt, G. and Lavallée, D.: Effect of annual signals on geodetic velocity, J. Geophys. Res., 107, B7, 2145, doi:10.1029/2001JB000570, 2002. 1031

Boehm, J., Niell, A. E., Tregoning, P., and Schuh, H.: Global Mapping Functions (GMF): a new empirical mapping function based on numerical weather model data, Geophys. Res. Lett., 33, L07304, doi:10.1029/2005GL025546, 2006. 1042

Boehm, J., Heinkelmann, R., and Schuh, H.: Short Note: a global model of pressure and temperature for geodetic applications, J. Geodesy, 81, 679–683, doi:10.1007/s00190-007-0135-3, 2007. 1042

Bouin, M. N. and Wöppelmann, G.: Land motion estimates from GPS at tide gauges: a geophysical evaluation, Geophys. J. Int., 180, 193–209, doi:10.1111/j.1365-246X.2009.04411.x, 2010. 1027, 1037, 1052

Buble, G., Bennett, R. A., and Hreinsdottir, S.: Tide gauge and GPS measurements of crustal motion and sea level rise along the eastern margin of Adria, J. Geophys. Res., 115, B02404, doi:10.1029/2008JB006155, 2010. 1027

Utsu, T.: Catalog of Damaging Earthquakes in the World (Through 1989), 1990. 1034, 1035

Cleveland, R. B., Cleveland, W. S., McRae, J. E., and Terpenning, I.: STL: A seasonal-trend decomposition procedure based on Loess, Journal of Official Statistics, 6, 3–73, 1990. 1030

Collilieux, X. and Wöppelmann, G.: Global sea-level rise and its relation to the terrestrial reference frame, J. Geodesy, 85, 9–22, doi:10.1007/s00190-010-0412-4, 2011. 1027

Collilieux, X., Metivier, L., Altamimi, Z., van Dam, T., and Ray, J.: Quality assessment of GPS reprocessed terrestrial reference frame, GPS Solut., 15, 219–231, doi:10.1007/s10291-010-0184-6, 2011. 1027

Dill, R.: Hydrological model LSDM for operational Earth rotation and gravity field variations, Scientific Technical Report, GFZ Potsdam, STR08/09, 35 pp., 2008. 1033, 1036

Dow, J., Neilan, R., and Rizos, C.: The international GNSS service in a changing landscape of global navigation satellite systems, J. Geodesy 83, 191–198, doi:10.1007/s00190-008-0300-3, 2009. 1029

EM-DAT: The OFDA/CRED International Disaster Database, Université Catholique de Louvain, Belgium, Brussels, available at: http://www.emdat.be, 2011. 1036

Emery, K. O. and Aubrey, D. G.: Sea levels, land levels, and tide gauges, Springer, 1991. 1035

Esquivel, R., Hernández, A., and Zermeño, M.: GPS for Subsidence Detection, the Case Study of Aguascalientes, in: Geodetic Deformation Monitoring: from Geophysical to Engineering Roles, International Association of Geodesy Symposia, Springer, 131, 254–258, doi:10.1007/978-3-540-38596-7_31, 2006. 1051

Ge, M., Gendt, G., Dick, G., and Zhang, F. P.: Improving carrier-phase ambiguity resolution in global GPS, J. Geodesy, 79, 103–110, doi:10.1007/s00190-005-0447-0, 2005. 1029

Ge, M., Gendt, G., Dick, G., Zhang, F. P., and Rothacher, M.: A new data processing strategy for huge GNSS global networks, J. Geodesy, 80, 199–203. doi:10.1007/s00190-006-0044-x, 2006. 1028

Gendt, G., Dick, G., Mai, W., Nischan, T., and Sommerfeld, W.: Nutzerhandbuch zum Programmsystem EPOS. P.V2 (Earth Parameters and Orbit determination System) für die Analyse von GPS-daten, GeoForschungsZentrum Potsdam, Bereich "Rezente Kinematik und Dynamik der Erde", 18 February 1994. 1028

Isoda, Y., Kitamura, F., and Murakami, T.: Interannual variations of the yearly mean sea level around the Japanese islands, Bulletin of Fisheries Sciences, 55, 85–95, 2004. 1035

Kaniuth, K., Häfele, P., and Sánchez, L.: Subsidence of the permanent GPS station Bogotá, in: Vertical Reference Systems. IAG Symposia, edited by: Drewes, H., Dodson, A., Fortes, L. P., Sánchez, L., and Sandoval, P., Springer, 124, 56–59, 2002. 1034

King, M. A. and Watson, C. S.: Long GPS coordinate time series: multipath and geometry effects, J. Geophys. Res., 115, B04403, doi:10.1029/2009JB006543, 2010. 1027

Kurtenbach, E., Mayer-Gürr, T., and Eicker, A.: Deriving daily snapshots of the Earth's gravity field from GRACE L1B data using Kalman filtering, Geophys. Res. Lett., 36, L17102, doi:10.1029/2009GL039564, 2009. 1036

Larsen, C. F., Motyka, R. J., Freymueller, J. T., Echelmeyer, K. A., Ivins, E. R.: Rapid uplift of Southern Alaska caused by recent ice loss, Geophys. J. Int., 158, 1118–1133, doi:10.1111/j.1365-246X.2004.02356.x, 2004. 1036

McCarthy, D. and Petit, G. (eds.): IERS Conventions (2003), IERS Technical Note 32, 2004. 1028, 1042

Sanchez, L. and Bosch, W.: The role of the TIGA project in the unification of classical height systems, in: Geodetic Reference Systems, edited by: Drewes H., IAG Symposia, vol. 134, Springer, 285–290, 2009. 1027

Schmid, R., Steigenberger, P., Gendt, G., Ge, M., and Rothacher, M.: Generation of a consistent absolute phase-center correction model for GPS receiver and satellite antennas, J. Geodesy, 81, 781–798, doi:10.1007/s00190-007-0148-y, available at: ftp://igscb.jpl.nasa.gov/pub/station/general/igs05.atx, last access: 15 January 2009, 2007. 1042

SED

4, 1025–1067, 2012

Reprocessed GPS station height time series

S. Rudenko et al.

Schöne, T., Schön, N., and Thaller, D.: IGS tide gauge benchmark monitoring pilot project (TIGA): scientific benefits, J. Geodesy, 83, 249–261, doi:10.1007/s00190-008-0269-y, 2009. 1026

van Dam, T. M.: Crustal displacements due to continental water loading, Geophys. Res. Lett., 28, 651–654, 2001. 1035

van Dam, T. M.: NCEP derived 6-hourly, global surface displacements at 2.5 × 2.5 degree spacing, updated October 2010, available at: http://geophy.uni.lu/ncep-loading.html, last access: 23 February 2012. 1036

van Dam, T. M., Blewitt, G., and Heflin, M.: Detection of atmospheric pressure loading using the global positioning system, J. Geophys. Res., 99, 939–950, 1994. 1036

Verbesselt, J., Hyndman, R., Newnham, G., and Culvenor, D.: Detecting trend and seasonal changes in satellite image time series, Remote Sens. Environ., 114, 106–115, doi:10.1016/j.rse.2009.08.014, 2010. 1030

Verdonck, D.: Contemporary vertical crustal deformation in Cascadia, Tectonophysics, 417, 221–230, 2006. 1031

Wöppelmann, G., Letetrel, C., Santamaria, A., Bouin, M.-N., Collilieux, X., Altamimi, Z., Williams, S. D. P., and Martin Miguez, B.: Rates of sea-level change over the past century in a geocentric reference frame Geophys. Res. Lett., 36, L12607, doi:10.1029/2009GL038720, 2009. 1027

Wu, J. T., Wu, S. C., Hajj, G. A., Bertiger, W. I., and Lichten, S. M.: Effects of antenna orientation on GPS phase, Manuscr. Geodaet, 18, 91–98, 1993. 1042

Zhang, F. P., Wünsch, J., van Dam, T., Gendt, G., Ge, M., and Schöne, T.: Vertical Crustal Motion at Tide Gauges Derived by Analyzing GPS Time Series, GeoForschungsZentrum Potsdam Scientific Technical Report STR08/03, 106 pp., 2008. 1026, 1037, 1052

Table 1. Input data, reference frames and models used for GPS data processing.

Observation data	
Basic observable	ionosphere-free linear combination, undifferenced carrier phases and pseudo-ranges
Sampling rate	5 min
Elevation cut-off angle	7°
Elevation depended weighting	$1/2\sin(e)$ for $e < 30^\circ$, 1 for $e \geq 30^\circ$
Measurement models	
Satellite antenna to center of mass offsets	spacecraft-specific z-offsets and block-specific x- and y-offsets from file igs05.atx (Schmid et al., 2007)
Phase centre variations (PCV)	absolute model
PCV for receiver and satellite	file igs05.atx (Schmid et al., 2007)
Antenna radome calibrations	applied, if given in file igs05.atx (Schmid et al., 2007), otherwise the radome effect is neglected and instead standard antenna model (radome => NONE) is used
GPS satellite attitude model	GPS satellite yaw attitude model (Bar-Sever, 1996) based on nominal yaw rates
RHC phase rotation correction	phase wind-up applied (Wu et al., 1993)
Marker to antenna eccentricity	dN, dE, dU eccentricities from site logs applied
Troposphere modeling	empirical Global Pressure and Temperature (GPT) model (Boehm et al., 2007), Saastamoinen "dry" and "wet" model for zenith delay, Global Mapping Function (GMF) (Boehm et al., 2006)
Ionosphere	first order effect
Tidal corrections	solid earth tide, permanent tide: applied in tide model, solid Earth pole tide, ocean tide loading (FES2004 model) (McCarthy et al., 2003) ocean tide geocenter: coefficients corrected for center of mass motion of whole Earth
Non-tidal loadings	atmospheric pressure, ocean bottom pressure, surface hydrology – all not applied
Earth orientation variations	ocean tidal: diurnal and semidiurnal variations in x, y-pole coordinates and UT1 applied according to (McCarthy et al., 2003)
Reference frames	
Inertial reference frame	geocentric, mean equator and equinox of January 1.5, 2000 (J2000.0)
Terrestrial reference frame	ITRF2005 (Altamimi et al., 2007) as a priori one
Reference frame interconnection	IAU2000A Precession-Nutation model, subdaily nutation with periods less than two days (McCarthy et al., 2003)
Earth Orientation Parameters	IERS EOP 05 C04 as initial ones, solved polar motion x, y and length-of day (LOD)
Orbit models	
Geopotential model	EIGEN-GL04S1 (up to $n = m = 12$) with temporal variations of C_{20}, C_{30}, C_{40}
Tidal variations in geopotential	solid earth tides, ocean tides, solid Earth pole tide (McCarthy et al., 2003)
Third-body attraction	Sun, Moon, Mercury, Venus, Mars, Jupiter, Saturn, Uranus, Neptune, Pluto (point masses), JPL Planetary Ephemeris DE405
Solar radiation pressure	a priori GPSM-XYZ.1 model, Earth shadow model: penumbra, Moon shadow model,
Relativistic effects	Schwarzschild and Lense-Thirring dynamical correction, gravitational time delay (McCarthy et al., 2003)
Numerical integration of orbit	single step Everhart integrator, direct integration of second-order equations with variable, automatically controlled integration step, arc length: 24 h
Numerical integration of variation equations	multistep step Stoermer-Cowell integrator with direct integration of second-order equations with fixed integration step using Cowell-Kulikov starter procedure, arc length: 24 h

SED
4, 1025–1067, 2012

Table 2. Linear height trends at GPS stations. The table contains all stations from the TIGA reprocessing campaign with time series larger than 2.5 yr from which a reasonable linear trend could be determined. Time series which showed large gaps were left out, as were station with obvious jumps or trend changes. Some of these examples were treated above. A seasonal trend was removed for all stations. Atmospheric corrections were not applied. The station longitude and latitude are given in degrees, arc minutes and arc seconds. The beginning and the end of the time series are given as the GPS week number. The length of the time series is given in years.

Station	Name	Lon	Lat	Trend (mm yr^{-1})	Begin	End	Length
0194	Sakata, Japan	139 32 51.6	39 11 8.0	0.9 ± 0.03	939	1459	10.0
ABER	Aberdeen, UK	357 55 11.2	57 8 38.4	1.69 ± 0.02	976	1459	9.3
AJAC	Ajaccio, France	8 45 45.4	41 55 38.8	0.31 ± 0.02	1045	1446	7.7
ALAC	Alicante, Spain	359 31 7.6	38 20 20.1	0.23 ± 0.01	1021	1459	8.4
ALGO	Algonquin Park, Canada	281 55 43.1	45 57 20.9	3.47 ± 0.02	939	1459	10.0
ALIC	Alice Springs, Australia	133 53 7.9	–23 40 12.4	0.38 ± 0.03	939	1459	10.0
ALME	Almeria, Spain	357 32 26.0	36 51 9.1	1.4 ± 0.03	1094	1459	7.0
ALRT	Alert, Canada	297 39 34.3	82 29 39.5	5.15 ± 0.03	1175	1459	5.5
ANDE	Andenes, Norway	16 8 5.3	69 19 33.8	2.48 ± 0.04	1096	1424	6.3
ANDO	Andenes, Norway	16 0 30.6	69 16 41.9	2.49 ± 0.03	939	1424	9.3
ANKR	Ankara, Turkey	32 45 30.5	39 53 14.5	−0.73 ± 0.05	939	1455	9.9
ANTA	Antalya, Turkey	30 36 33.9	36 49 42.6	−2.27 ± 0.18	1245	1455	4.0
AOML	Key Biscayne, FL, USA	279 50 16.1	25 44 4.9	0.5 ± 0.03	939	1265	6.3
AREQ	Arequipa, Peru	288 30 25.9	–16 27 55.9	3.81 ± 0.02	1138	1459	6.2
ARTU	Arti Ekaterinburg, Russia	58 33 37.6	56 25 47.4	0.9 ± 0.04	1021	1459	8.4
AUCK	Whangaparaoa No3, NZ	174 50 3.8	–36 36 10.2	−1.55 ± 0.04	939	1459	10.0
BAHR	Manama, Bahrain	50 36 29.3	26 12 32.9	0.53 ± 0.02	939	1459	10.0
BAIE	Baie Comeau, Canada	291 44 12.0	49 11 12.6	3.49 ± 0.03	1147	1459	6.0
BAKE	Baker Lake, Canada	263 59 51.6	64 19 4.2	10.82 ± 0.04	1147	1438	5.6
BILI	Bilibino, Russia	166 26 16.7	68 4 34.1	0.28 ± 0.03	1025	1459	8.3
BISH	Bishkek, Kyrgystan	74 35 39.1	42 52 32.1	−1.42 ± 0.05	939	1359	8.1
BJFS	Beijing, China	115 53 32.9	39 36 31.0	3.47 ± 0.05	1032	1459	8.2
BOGT	Bogota, Colombia	285 55 8.6	4 38 24.3	−44.21 ± 0.19	942	1459	9.9
BOR1	Borowice, Poland	17 4 24.4	52 16 37.0	−0.04 ± 0.01	1192	1459	5.1

SED
4, 1025–1067, 2012

Table 2. Continued.

Station	Name	Lon	Lat	Trend (mm yr^{-1})	Begin	End	Length
BRAZ	Brasilia, Brazil	312 7 19.7	–15 56 50.9	−0.18 ± 0.05	940	1459	10.0
BRMU	Bermuda, UK	295 18 13.4	32 22 13.4	−0.54 ± 0.03	939	1459	10.0
BRUS	Brussels, Belgium	4 21 33.2	50 47 52.1	0.78 ± 0.03	939	1459	10.0
BUR1	Burnie, Tasmania	145 54 53.4	–41 3 0.2	−0.24 ± 0.03	1004	1412	7.8
CABL	Port Orford, OR, USA	235 26 12.0	42 50 10.0	−0.06 ± 0.04	1188	1459	5.2
CAGL	Cagliari, Italy	8 58 21.9	39 8 9.3	−0.15 ± 0.03	939	1459	10.0
CANT	Santander, Spain	356 12 7.0	43 28 19.1	0.38 ± 0.04	1094	1459	7.0
CART	Cartagena, Colombia	284 27 58.1	10 23 28.8	−2.12 ± 0.07	1047	1456	7.9
CAS1	Casey, Antarctica	110 31 10.9	–66 17 0.1	−0.41 ± 0.08	1088	1453	7.0
CASC	Cascais, Portugal	350 34 53.3	38 41 36.3	0.19 ± 0.03	955	1459	9.7
CCV3	Cape Canaveral, FL, USA	279 27 17.2	28 27 36.8	0.23 ± 0.22	969	1411	8.5
CEDU	Ceduna, Australia	133 48 35.4	–31 51 60.0	−1.07 ± 0.03	944	1459	9.9
CFAG	Caucete, Argentina	291 46 2.5	–31 36 7.8	−0.69 ± 0.04	939	1459	10.0
CHA1	Charleston, SC, USA	280 9 25.7	32 45 27.2	−0.73 ± 0.04	988	1245	4.9
CHAT	Chatham Island, NZ	183 26 3.0	–43 57 20.8	−0.37 ± 0.02	939	1459	10.0
CHUM	Chumysh, Kazakhstan	74 45 3.9	42 59 54.6	0.4 ± 0.02	939	1459	10.0
CHUR	Churchill, Canada	265 54 40.6	58 45 32.7	9.67 ± 0.03	939	1459	10.0
CKIS	Rarotonga, NZ	200 11 57.8	–21 12 3.7	0.04 ± 0.03	1131	1459	6.3
COCO	CocosIsland, Australia	96 50 2.3	–12 11 18.0	−0.68 ± 0.04	939	1459	10.0
CONZ	Concepcion, Chile	286 58 28.3	–36 50 37.5	0.39 ± 0.11	1170	1459	5.6
CRO1	St. Croix, Virgin Isl., USA	295 24 56.4	17 45 24.8	−1.87 ± 0.03	939	1459	10.0
CSAR	Ceasarya, Israel	34 53 24.7	32 29 17.7	0.5 ± 0.04	1263	1459	3.8
DAEJ	Taejon, Korea	127 22 28.1	36 23 57.9	1.51 ± 0.07	1001	1459	8.8
DARW	Darwin, Australia	131 7 57.9	–12 50 37.3	−0.17 ± 0.07	1242	1457	4.1
DAV1	Davis, Antarctica	77 58 21.4	–68 34 38.4	−1.92 ± 0.03	1038	1459	8.1
DRAG	Metzoki Dragot, Israel	35 23 31.4	31 35 35.5	3.15 ± 0.03	1033	1459	8.2
DRAO	Penticton, Canada	240 22 30.1	49 19 21.4	−0.56 ± 0.03	1188	1459	5.2
DUBO	Lac du Bonnet, Canada	264 8 1.7	50 15 31.7	2.13 ± 0.06	1288	1459	3.3
DUM1	Dumont, Antarctica	140 0 7.0	–66 39 54.3	−2.11 ± 0.02	939	1459	10.0
DUNT	Dunedin, NZ	170 37 45.9	–45 48 51.5	−1.63 ± 0.02	1029	1459	8.3
EIJS	Eijsden, Nederlands	5 41 1.0	50 45 29.7	3.58 ± 0.06	939	1459	10.0
ESTI	Esteli, Nicaragua	273 38 16.3	13 5 58.3	5.06 ± 0.06	1061	1207	2.8
FAIR	Fairbanks, AL, USA	212 30 2.7	64 58 40.8	2.52 ± 0.06	1188	1459	5.2

SED
4, 1025–1067, 2012

Table 2. Continued.

Station	Name	Lon	Lat	Trend (mm yr^{-1})	Begin	End	Length
FLIN	Flin Flon, Canada	258 1 19.1	54 43 32.1	3.53 ± 0.03	1288	1459	3.3
FORT	Fortaleza, Brazil	321 34 27.8	–3 52 38.8	1.4 ± 0.06	1188	1370	3.5
FREE	Freeport, Bahamas	281 0 26.8	26 42 9.1	1.78 ± 0.07	1013	1137	2.4
FTS1	Fort Stevens, OR, USA	236 2 38.1	46 12 17.6	2.82 ± 0.02	939	1459	10.0
GAL1	Galveston, TX, USA	265 15 47.5	29 19 47.6	−4.76 ± 0.05	939	1226	5.5
GALA	Galapagos Isl., Ecuador	269 41 47.0	0 44 33.7	−2.59 ± 0.09	939	1192	4.9
GENO	Genova, Italy	8 55 16.1	44 25 9.8	−0.48 ± 0.04	967	1459	9.5
GETI	Geting, Malaysia	102 6 19.7	6 13 34.3	3.39 ± 0.02	990	1186	3.8
GLPT	Gloucester Point, VA, USA	283 30 2.0	37 14 54.8	−2.61 ± 0.03	939	1385	8.6
GLSV	Kiev, Ukraine	30 29 48.2	50 21 51.1	0.2 ± 0.03	949	1459	9.8
GODE	Greenbelt, ML, USA	283 10 23.4	39 1 18.2	−1.56 ± 0.03	939	1459	10.0
GOLD	Goldstone, CA, USA	243 6 38.7	35 25 30.6	0.25 ± 0.09	1088	1459	7.1
GOPE	Ondrejov, CZ	14 47 8.2	49 54 49.3	−1.44 ± 0.04	1192	1459	5.1
GRAS	Grasse, France	6 55 14.1	43 45 17.1	0.59 ± 0.01	939	1459	10.0
GRAZ	Graz, Austria	15 29 36.5	47 4 1.7	0.43 ± 0.02	939	1459	10.0
GUAM	Dededo, Guam	144 52 6.1	13 35 21.6	−0.01 ± 0.04	1138	1459	6.2
GUAT	Guatemala	269 28 47.3	14 35 25.5	1.04 ± 0.06	1072	1459	7.4
HELG	Helgoland, Germany	7 53 35.1	54 10 28.1	1.04 ± 0.02	1035	1459	8.2
HILO	Hilo, Hawaii, USA	204 56 50.3	19 43 9.1	−1.66 ± 0.02	939	1454	9.9
HLFX	Halifax, Canada	296 23 19.4	44 41 0.8	−1.13 ± 0.02	1147	1459	6.0
HNLC	Honolulu, Hawaii, USA	202 8 7.6	21 18 11.8	−0.66 ± 0.04	939	1459	10.0
HNPT	Horn Point, ML, USA	283 52 10.7	38 35 19.7	−2.51 ± 0.02	1038	1459	8.1
HOB2	Hobart, Australia	147 26 19.4	–42 48 17.0	−0.53 ± 0.04	1038	1459	8.1
HOFN	Hoefn, Iceland	344 48 7.5	64 16 2.3	13.52 ± 0.06	1138	1459	6.2
HOLM	Holman, Canada	242 14 19.5	70 44 10.7	2.63 ± 0.03	1129	1459	6.3
HRAO	Hartebeesthoek, South Africa	27 41 13.1	–25 53 24.4	−0.72 ± 0.02	942	1457	9.9
IISC	Bangalore, India	77 34 13.3	13 1 16.2	0.06 ± 0.03	939	1459	10.0
INEG[1]	Aguascalientes, Mexico	257 42 56.9	21 51 22.2	−87.66 ± 0.28	1038	1158	2.3
IRKT	Irkutsk, Russia	104 18 58.5	52 13 8.5	1.26 ± 0.03	939	1459	10.0
JOZE	Josefoslaw, Poland	21 1 53.5	52 5 50.2	1 ± 0.01	939	1459	10.0
JPLM	Pasadena, CA, USA	241 49 36.4	34 12 17.4	0.91 ± 0.06	939	1459	10.0
KARR	Karratha, Australia	117 5 49.9	–20 58 53.1	0.55 ± 0.04	939	1459	10.0
KELS	Kelso, WA, USA	237 6 14.2	46 7 5.4	−0.53 ± 0.02	939	1444	9.7
KEN1	Kenai, AL, USA	208 38 59.3	60 40 30.3	9.17 ± 0.12	939	1443	9.7
KERG	Kerguelen	70 15 19.9	–49 21 5.3	0.99 ± 0.02	1188	1459	5.2

SED
4, 1025–1067, 2012

Table 2. Continued.

Station	Name	Lon	Lat	Trend (mm yr^{-1})	Begin	End	Length
KGN0	Koganei, Japan	139 29 18.7	35 42 24.4	0.83 ± 0.02	1128	1368	4.6
KIRI	Betio, Kiribati	172 55 22.4	1 21 16.5	−2.03 ± 0.06	1177	1459	5.4
KIRU	Kiruna, Sweden	20 58 6.4	67 51 26.5	6.48 ± 0.07	939	1459	10.0
KIT3	Kitab, Uzbekistan	66 53 7.6	39 8 5.2	−0.95 ± 0.05	939	1459	10.0
KODK	Kodiak, AL, USA	207 29 55.0	57 44 6.4	8.82 ± 0.1	1039	1385	6.7
KOSG	Kootwijk, Netherlands	5 48 34.7	52 10 42.3	−0.44 ± 0.02	939	1459	10.0
KOUR	Kourou, French Guyana	307 11 38.5	5 15 7.9	−0.32 ± 0.09	1088	1459	7.1
KSTU	Krasnojarsk, Russia	92 47 37.8	55 59 35.7	1.13 ± 0.04	949	1289	6.5
KUNM	Kunming, China	102 47 49.9	25 1 46.3	−0.08 ± 0.06	978	1459	9.3
KUUJ	Kuujjuarapik, Canada	282 15 16.4	55 16 42.1	11.52 ± 0.06	1173	1445	5.2
KWJ1	Kwajalein	167 43 48.9	8 43 19.9	−1.63 ± 0.14	939	1176	4.6
KYW1	Key West, FL, USA	278 20 49.1	24 34 56.2	−1.01 ± 0.01	939	1448	9.8
LAE1	Lae, Papua New Guinea	146 59 35.5	−6 40 25.3	−5.39 ± 0.04	1095	1384	5.6
LAGO	Lagos, Portugal	351 19 53.8	37 5 56.2	−0.76 ± 0.02	1056	1459	7.8
LAMP	Lampedusa, Italy	12 36 20.4	35 29 59.2	0.42 ± 0.02	1002	1459	8.8
LAUT	Lautoka, Fiji	177 26 47.7	−17 36 31.7	−0.19 ± 0.11	1141	1459	6.1
LHAS	Lhasa, Tibet	91 6 14.4	29 39 26.4	0.82 ± 0.03	939	1412	9.1
LPGS	La Plata, Argentina	302 4 3.7	−34 54 24.3	2.78 ± 0.05	939	1459	10.0
LROC	La Rochelle, France	358 46 50.5	46 9 32.2	0.29 ± 0.03	1141	1459	6.1
LYTT	Lyttelton, NZ	172 43 20.0	−43 36 21.0	-0.95 ±0.02	1037	1459	8.1
MAC1	MacQuarie, Australia	158 56 9.0	−54 29 58.3	−2.84 ± 0.03	939	1459	10.0
MADR	Madrid (Robledo), Spain	355 45 1.2	40 25 45.0	−0.22 ± 0.08	939	1459	10.0
MALI	Malindi, Kenya	40 11 39.8	-2 59 45.3	−0.87 ± 0.11	939	1459	10.0
MAR6	Maartsbo, Sweden	17 15 30.7	60 35 42.5	7.62 ± 0.01	999	1459	8.8
MARS	Marseille, France	5 21 13.6	43 16 43.6	0.33 ± 0.02	966	1459	9.5
MAS1	Maspalomas, Gran Canaria	344 22 0.2	27 45 49.5	−0.62 ± 0.04	1038	1459	8.1
MATE	Matera, Italy	16 42 16.0	40 38 56.9	1.05 ± 0.02	939	1459	10.0
MAW1	Mawson, Antarctica	62 52 14.6	−67 36 17.2	−0.95 ± 0.01	939	1459	10.0
MBAR	Mbarara, Uganda	30 44 16.4	0 36 5.3	2.68 ± 0.05	1123	1455	6.4
MDO1	Mcdonald, TX, USA	255 59 6.0	30 40 49.8	0.27 ± 0.03	939	1459	10.0
METS	Metsahovi, Finland	24 23 43.1	60 13 2.9	4.7 ± 0.01	939	1459	10.0
MIL1	Milwaukee, WI, USA	272 6 41.6	43 0 9.1	−3.4 ± 0.02	939	1401	8.9
MKEA	Mauna Kea, Hawaii	204 32 37.2	19 48 4.9	−2.46 ± 0.03	939	1459	10.0
MOB1	Mobile, AL, USA	271 58 33.2	30 13 39.1	−4.03 ± 0.05	939	1459	10.0

SED
4, 1025–1067, 2012

Table 2. Continued.

Station	Name	Lon	Lat	Trend (mm yr^{-1})	Begin	End	Length
MPLA	Mar del Plata, Argentina	302 28 7.7	–38 2 8.3	–2.26 ± 0.14	1187	1455	5.2
MQZG	McQueens Valley, NZ	172 39 16.9	–43 42 9.8	–2.11 ± 0.04	1029	1459	8.3
NAIN	Nain, Canada	298 18 40.6	56 32 13.1	4.09 ± 0.03	1197	1459	5.0
NANO	Nanoose Bay, Canada	235 54 48.7	49 17 41.3	0.6 ± 0.03	939	1459	10.0
NCDK	Duck, NC, USA	284 14 55.5	36 10 55.4	–3.16 ± 0.15	1267	1417	2.9
NEAH	Neah Bay, WA, USA	235 22 30.3	48 17 52.3	3.96 ± 0.02	939	1459	10.0
NEIA	Cananeia, Brazil	312 4 30.1	–25 1 12.9	0.49 ± 0.01	1172	1458	5.5
NEWL	Newlyn, UK	354 27 26.0	50 6 10.9	–0.17 ± 0.02	977	1458	9.3
NEWP	Newport, USA	235 56 17.2	44 35 6.1	1.57 ± 0.02	947	1418	9.1
NICO	Nicosia, Cyprus	33 23 47.2	35 8 27.6	0.8 ± 0.04	939	1459	10.0
NKLG	N'Koltang, Gabon	9 40 19.6	0 21 14.1	–0.03 ± 0.03	1055	1458	7.8
NOUM	Noumea, New Caledonia	166 24 36.7	–22 16 11.5	–3.06 ± 0.05	939	1419	9.2
NPLD	Teddington, UK	359 39 37.3	51 25 15.5	0.61 ± 0.04	1095	1458	7.0
NRC1	Ottawa, Canada	284 22 34.2	45 27 15.0	3.49 ± 0.01	939	1459	10.0
NRIL	Norilsk, Russia	88 21 35.2	69 21 42.6	2.24 ± 0.04	1079	1459	7.3
NSTG	North Shields, UK	358 33 36.5	55 0 26.7	0.7 ± 0.02	1213	1459	4.7
NVSK	Novosibirsk, Russia	83 14 7.6	54 50 26.2	0.63 ± 0.05	1070	1459	7.5
NYA1	Ny Alesund, Norway	11 51 55.1	78 55 46.4	8.54 ± 0.04	948	1459	9.8
NYAL	Ny Alesund, Norway	11 51 54.3	78 55 46.5	8.81 ± 0.04	945	1459	9.9
OBE2	Oberpfaffenhofen 2	11 16 47.5	48 5 10.2	0.88 ± 0.05	1126	1457	6.4
OBER	Oberpfaffenhofen	11 16 47.5	48 5 10.2	–0.67 ± 0.1	939	1115	3.4
ONSA	Onsala, Sweden	11 55 31.9	57 23 43.1	1.9 ± 0.05	939	1459	10.0
OUS2	Dunedin, NZ	170 30 39.4	–45 52 10.1	–1.38 ± 0.03	1164	1459	5.7
P102	Okushiri, Japan	139 29 21.1	42 4 43.6	–4.12 ± 0.03	1214	1459	4.7
P103	Aomori, Japan	140 51 33.1	40 53 51.0	1.81 ± 0.01	1212	1459	4.8
P104	Oga, Japan	139 42 12.4	39 56 31.6	3.66 ± 0.02	1221	1459	4.6
P108	Miura, Japan	139 36 55.9	35 9 36.6	–1.71 ± 0.02	1212	1459	4.8
P109	Ogi, Japan	138 16 52.5	37 48 53.1	2.46 ± 0.02	1221	1459	4.6
P110	Kashiwazaki, Japan	138 30 30.7	37 21 23.6	–2.17 ± 0.23	1224	1458	4.5
P112	Mikuni, Japan	136 8 55.8	36 15 16.5	–0.95 ± 0.01	1221	1459	4.6
P114	Nishiizu, Japan	138 45 51.1	34 48 24.8	–2.34 ± 0.01	1222	1459	4.6
P115	Yaizu, Japan	138 19 38.7	34 52 14.4	–2.92 ± 0.06	1222	1459	4.6
P116	Tokoname, Japan	136 49 25.8	34 54 14.3	8.27 ± 0.06	1222	1459	4.6

SED
4, 1025–1067, 2012

Table 2. Continued.

Station	Name	Lon	Lat	Trend (mm yr^{-1})	Begin	End	Length
P117	Kainan, Japan	135 11 29.5	34 8 38.9	4.34 ± 0.01	1222	1459	4.6
P118	Iwami, Japan	134 18 57.4	35 35 37.3	−0.43 ± 0.01	1223	1459	4.5
P119	Susa, Japan	131 36 16.7	34 37 39.3	0.49 ± 0.02	1213	1459	4.7
P120	Nakatosa, Japan	133 14 36.6	33 20 0.6	7.03 ± 0.07	1222	1459	4.6
P124	Tinen, Japan	127 49 28.8	26 10 46.1	0.15 ± 0.03	1222	1459	4.6
P201	Wakkanai, Japan	141 41 7.2	45 24 28.2	1.51 ± 0.02	1212	1459	4.8
P202	Abashiri, Japan	144 17 8.9	44 1 9.9	1.95 ± 0.02	1221	1459	4.6
P203	Kushiro, Japan	144 22 17.0	42 58 32.1	1.96 ± 0.09	1263	1459	3.8
P204	Hakodate, Japan	140 43 28.3	41 46 54.0	1.29 ± 0.03	1214	1459	4.7
P206	Tateyama, Japan	139 49 29.7	34 55 7.7	−1.12 ± 0	1223	1459	4.5
P209	Hamada, Japan	132 3 58.4	34 53 50.3	−0.67 ± 0.01	1223	1459	4.5
P211	Nichinan, Japan	131 24 33.5	31 34 37.1	−0.68 ± 0.05	1220	1459	4.6
P212	Naha, Japan	127 39 54.7	26 12 48.0	−0.18 ± 0.01	1222	1459	4.6
P213	Ogasawara, Japan	142 11 40.6	27 5 38.2	0.1 ± 0.08	1215	1459	4.7
PALM	Palmer Station, Antarctica	295 56 56.0	–64 46 30.3	3.91 ± 0.06	965	1446	9.3
PAPE	Papeete, Tahiti	210 25 38.2	–17 31 59.1	−0.12 ± 0.03	1253	1459	4.0
PARC	Punta Arenas, Chile	289 7 12.4	–53 8 13.0	−1.26 ± 0.02	990	1459	9.0
PBL1	Point Blunt, CA, USA	237 34 51.8	37 51 11.0	−0.15 ± 0.07	939	1261	6.2
PDEL	Ponta Delgada, Azores	334 20 14.0	37 44 51.9	−2.08 ± 0.03	1058	1459	7.7
PERT	Perth, Australia	115 53 6.9	–31 48 7.1	−6.3 ± 0.05	939	1459	10.0
PETP	Petropavlovsk-Kamchatskij	158 36 25.5	53 4 0.2	−4.15 ± 0.07	978	1459	9.3
PGC5	Sidney, Canada	236 32 55.9	48 38 54.7	−1.36 ± 0.16	1315	1459	2.8
PIMO	Manila, Philippines	121 4 39.8	14 38 8.6	0.8 ± 0.01	1200	1459	5.0
PLO3	Point Loma, CA, USA	242 45 25.1	32 39 55.5	−0.01 ± 0.09	939	1382	8.5
PLUZ	Las Palmas, Canary Isl.	344 35 32.6	28 8 48.2	−1.05 ± 0.06	1265	1438	3.3
PNGM	Lombrum, Papua New Guinea	147 21 57.6	–2 2 35.6	−1.64 ± 0.16	1164	1459	5.7
POHN	Pohnpei, Micronesia	158 12 36.4	6 57 35.8	−1.02 ± 0.05	1216	1459	4.7
POLV	Poltava, Ukraine	34 32 34.5	49 36 9.4	−0.25 ± 0.04	1119	1459	6.5
POR4	New Castle, NH, USA	289 17 25.7	43 4 15.7	0.88 ± 0.1	1056	1295	4.6
POTS	Potsdam, Germany	13 3 57.9	52 22 45.5	−0.63 ± 0.04	939	1459	10.0
PRDS	Calgary, Canada	245 42 23.4	50 52 16.9	0.7 ± 0.08	939	1459	10.0
QAQ1	Qaqortoq, Greenland	313 57 8.1	60 42 55.0	4.97 ± 0.06	1167	1459	5.6
RABT	Rabat, Morocco	353 8 44.6	33 59 53.2	−1.08 ± 0.03	1062	1459	7.6
RAMO	Mitzpe Ramon, Israel	34 45 47.3	30 35 51.4	1.08 ± 0.04	961	1459	9.6

SED
4, 1025–1067, 2012

Table 2. Continued.

Station	Name	Lon	Lat	Trend (mm yr^{-1})	Begin	End	Length
RED1	Reedy Point, DE, USA	284 25 48.1	39 33 41.2	−2.39 ± 0.07	996	1424	8.2
REYK	Reykjavik, Iceland	338 2 40.2	64 8 19.6	−3.08 ± 0.05	939	1459	10.0
REYZ	Reykjavik, Iceland	338 2 40.3	64 8 19.7	−1.09 ± 0.03	1170	1445	5.3
RIGA	Riga, Latvia	24 3 31.6	56 56 55.0	1.56 ± 0.03	999	1459	8.8
RIOG	Rio Grande, Argentina	292 14 56.0	–53 47 7.7	2.99 ± 0.05	939	1416	9.2
RWSN	Rawson, Argentina	294 53 33.9	–43 17 56.0	−0.01 ± 0.02	1046	1456	7.9
SAG1	Saginaw Bay, MI, USA	276 9 44.0	43 37 43.1	−3.04 ± 0.02	939	1454	9.9
SANT	Santiago, Chile	289 19 53.2	–33 9 1.0	3.17 ± 0.03	939	1459	10.0
SCH2	Schefferville, Canada	293 10 2.6	54 49 55.5	10.88 ± 0.03	939	1459	10.0
SCUB	Santiago de Cuba	284 14 15.7	20 0 43.4	0.12 ± 0.07	1050	1459	7.9
SEAT	Seattle, WA, USA	237 41 25.9	47 39 14.3	−0.2 ± 0.03	939	1459	10.0
SELD	Seldovia, AL, USA	208 17 36.0	59 26 44.6	10.21 ± 0.08	1085	1459	7.2
SFER	San Fernando, Spain	353 47 39.7	36 27 51.6	1.22 ± 0.03	991	1459	9.0
SHEE	Sheerness, UK	0 44 36.3	51 26 44.5	−0.32 ± 0.05	939	1459	10.0
SIO3	Scripps, CA, USA	242 44 58.5	32 51 52.9	2.54 ± 0.07	1038	1459	8.1
SKE0	Skellefteaa, Sweden	21 2 53.8	64 52 45.1	10.8 ± 0.06	1232	1459	4.4
SOFI	Sofia, Bulgaria	23 23 41.0	42 33 21.9	0.17 ± 0.02	939	1459	10.0
SOL1	Solomons Island, ML, USA	283 32 46.0	38 19 8.0	0.19 ± 0.34	939	1437	9.6
STJO	St. Johns, Canada	307 19 20.1	47 35 42.9	0.59 ± 0.02	939	1459	10.0
SUTH	Sutherland, South Africa	20 48 37.7	–32 22 48.8	−0.28 ± 0.02	953	1458	9.7
SUWN	Suwon-shi, Korea	127 3 15.3	37 16 31.9	0.61 ± 0.06	939	1459	10.0
SYOG	Syowa, Antarctica	39 35 1.5	–69 0 25.0	0.64 ± 0.04	939	1459	10.0
TERS	Terschelling, NL	5 13 9.8	53 21 45.9	0.8 ± 0.05	939	1459	10.0
THTI	Tahiti	210 23 36.8	–17 34 37.4	−0.89 ± 0.03	960	1459	9.6
THU3	Thule Airbase, Greenland	291 10 29.9	76 32 13.4	5.05 ± 0.04	1167	1459	5.6
TID1	Tidbinbilla, Australia	148 58 48.0	–35 23 57.1	0.22 ± 0.04	939	1459	10.0
TID2	Tidbinbilla, Australia	148 58 48.0	–35 23 57.1	0.36 ± 0.04	939	1453	9.9
TIDB	Tidbinbilla, Australia	148 58 48.0	–35 23 57.1	−0.93 ± 0.04	1088	1459	7.1
TIXI	Yakutia-Sakha, Russia	128 51 59.1	71 38 4.1	0.89 ± 0.02	978	1459	9.3
TLSE	Toulouse, France	1 28 51.2	43 33 38.5	−0.11 ± 0.04	1095	1459	7.0
TONG	Nuku Alofa, Tonga	184 49 14.8	–21 8 41.0	−1.07 ± 0.06	1154	1459	5.9
TORP	Torrance, CA, USA	241 40 9.8	33 47 52.1	−0.08 ± 0.04	939	1459	10.0
TOW2	Townsville, Queensland	147 3 20.5	–19 16 9.4	−0.54 ± 0.03	939	1459	10.0
TRAB	Trabzon, Turkey	39 46 32.0	40 59 41.0	0.38 ± 0.02	1039	1455	8.0

SED
4, 1025–1067, 2012

Table 2. Continued.

Station	Name	Lon	Lat	Trend (mm yr^{-1})	Begin	End	Length
TRDS	Trondheim, Norway	10 19 9.0	63 22 17.0	4.93 ± 0.03	1086	1459	7.2
TRO1	Tromsø, Norway	18 56 22.7	69 39 45.8	3.5 ± 0.05	948	1459	9.8
TRON	Trondheim, Norway	10 19 9.0	63 22 17.0	−9.5 ± 0.79	939	1050	2.1
TSEA	Anchorage, USA	210 6 18.1	61 11 14.4	3.53 ± 0.07	1016	1459	8.5
TSKB	Tsukuba, Japan	140 5 15.0	36 6 20.5	−0.14 ± 0.05	939	1459	10.0
TUKT	Tuktoyaktuk, Canada	227 0 20.3	69 26 17.6	−0.01 ± 0.02	1233	1459	4.3
TUVA	Funafuti, Tuvalu	179 11 47.6	-8 31 31.0	−0.01 ± 0.05	1142	1459	6.1
UCLU	Ucluelet, Canada	234 27 30.1	48 55 32.3	2.82 ± 0.09	1138	1459	6.2
ULAB	Ulaanbataar, Mongolia	107 3 8.4	47 51 54.2	0.83 ± 0.02	1087	1459	7.2
UNB1	Fredericton, Canada	293 21 29.9	45 57 0.8	0.61 ± 0.09	1123	1388	5.1
UNSA	Salta, Argentina	294 35 32.5	–24 43 38.8	−0.87 ± 0.06	1199	1459	5.0
USNO	US Naval Obs., WA, USA	282 56 1.6	38 55 8.3	−1.67 ± 0.02	939	1459	10.0
UZHL	Uzhgorod, Ukraine	22 17 51.4	48 37 55.1	0.14 ± 0.04	1016	1459	8.5
VAAS	Vaasa, Finland	21 46 14.3	62 57 40.3	8.66 ± 0.04	999	1459	8.8
VALD	Val d'Or, Canada	282 26 9.0	48 5 49.4	8.04 ± 0.04	1148	1459	6.0
VALE	Valencia, Spain	359 39 44.5	39 28 51.0	−1.33 ± 0.06	1094	1459	7.0
VANU	Port Vila, Vanuatu	168 18 54.5	–17 44 38.3	−2.87 ± 0.06	1183	1459	5.3
VARS	Vardoe, Norway	31 1 52.3	70 20 10.9	3.7 ± 0.04	1086	1459	7.2
VENE	Venezia, Italy	12 19 55.1	45 26 13.1	−1.04 ± 0.05	1138	1437	5.8
VESL	Vesleskarvet, Antarctica	357 9 29.6	–71 40 25.7	0.01 ± 0.1	970	1459	9.4
VILL	Villafranca, Spain	356 2 52.9	40 26 36.9	−1.75 ± 0.03	939	1459	10.0
VIMS	Wachapreague, VA, USA	284 18 46.8	37 36 30.1	−3.13 ± 0.02	939	1459	10.0
VIS0	Visby, Sweden	18 22 2.3	57 39 13.9	3.14 ± 0.03	999	1459	8.8
VTIS	Los Angeles, CA, USA	241 42 22.2	33 42 45.5	0.46 ± 0.07	987	1459	9.1
WARN	Warnemuende, Germany	12 6 5.1	54 10 11.2	0.48 ± 0.05	1205	1459	4.9
WGTN	Wellington, NZ	174 48 21.2	–41 19 24.4	−2.64 ± 0.02	939	1459	10.0
WGTT	Wellington, NZ	174 46 53.7	–41 17 25.6	−4.22 ± 0.02	1040	1459	8.1
WILL	Williams Lake, Canada	237 49 55.9	52 14 12.7	1.92 ± 0.03	939	1459	10.0
WIS1	Wisconsin Point, WI, USA	267 59 5.2	46 42 18.2	−0.88 ± 0.05	939	1453	9.9
WLAD	Wladyslawowo, Poland	18 25 7.5	54 47 48.3	0.26 ± 0.03	1215	1459	4.7
WSRT	Westerbork, NL	6 36 16.2	52 54 52.6	−0.6 ± 0.02	939	1459	10.0
WTZR	Wettzell, Germany	12 52 44.1	49 8 39.1	−0.08 ± 0.02	939	1459	10.0
WUHN	Wuhan, China	114 21 26.1	30 31 54.0	4.66 ± 0.09	939	1459	10.0

SED
4, 1025–1067, 2012

Table 2. Continued.

Station	Name	Lon	Lat	Trend (mm yr^{-1})	Begin	End	Length
YAKT	Yakutsk, Russia	129 40 49.1	62 1 51.5	−5.44 ± 0.34	992	1459	9.0
YAR1	Yaragadee, Australia	115 20 49.1	−29 2 47.6	−1.31 ± 0.07	939	1166	4.4
YELL	Yellowknife, Canada	245 31 9.5	62 28 51.2	6.2 ± 0.02	939	1459	10.0
YSSK	Yuzhno-Sakhalinsk, Russia	142 43 0.2	47 1 47.0	1.15 ± 0.02	1020	1459	8.4
ZECK	Zellenchuskaya, Russia	41 33 54.2	43 47 18.2	1.83 ± 0.02	939	1459	10.0
ZIMM	Zimmerwald, CH	7 27 55.0	46 52 37.6	1.67 ± 0.03	939	1459	10.0

[1] Subsidence at Aguascalientes (INEG) has been treated in Esquivel et al. (2006)

SED
4, 1025–1067, 2012

Table 3. Comparison of the vertical velocities (mm yr^{-1}) of some GPS stations of our solution with two recent solutions.

Station	Our solution	Bouin and Wöppelmann (2010) solution	Zhang et al. (2008) solution
ALRT	5.15 ± 0.03	5.46 ± 1.64	8.96 ± 0.05
BAHR	0.53 ± 0.02	0.93 ± 0.72	0.28 ± 0.01
CHUR	9.67 ± 0.03	10.77 ± 0.72	10.80 ± 0.04
FTS1	2.82 ± 0.02	3.00 ± 0.73	−0.89 ± 0.03
KEN1	9.17 ± 0.12	8.56 ± 0.76	12.66 ± 0.04
MAW1	−0.95 ± 0.01	−0.35 ± 0.72	3.20 ± 0.02
MOB1	−4.03 ± 0.05	−3.58 ± 0.76	−2.45 ± 0.04
NEAH	3.96 ± 0.02	3.82 ± 0.82	2.93 ± 0.02
NEWP	1.57 ± 0.02	1.61 ± 0.77	1.34 ± 0.01
NOUM	−3.06 ± 0.05	−2.68 ± 0.80	−0.05 ± 0.02
NYAL	8.81 ± 0.04	8.19 ± 0.73	8.32 ± 0.01
PARC	−1.26 ± 0.02	−1.39 ± 0.87	0.66 ± 0.05
PERT	−6.30 ± 0.05	−5.21 ± 0.73	−3.88 ± 0.02
PETP	−4.15 ± 0.07	−2.70 ± 0.88	−3.91 ± 0.02
SEAT	−0.20 ± 0.07	0.14 ± 0.81	−0.98 ± 0.02
SFER	1.22 ± 0.03	1.60 ± 0.89	2.00 ± 0.02
STJO	0.59 ± 0.02	−0.22 ± 0.72	−0.30 ± 0.01
SYOG	0.64 ± 0.04	2.75 ± 0.80	3.45 ± 0.02
TRO1	3.50 ± 0.05	3.43 ± 0.82	3.95 ± 0.02
WGTT	−4.22 ± 0.02	−3.94 ± 1.04	−1.64 ± 0.03

SED
4, 1025–1067, 2012

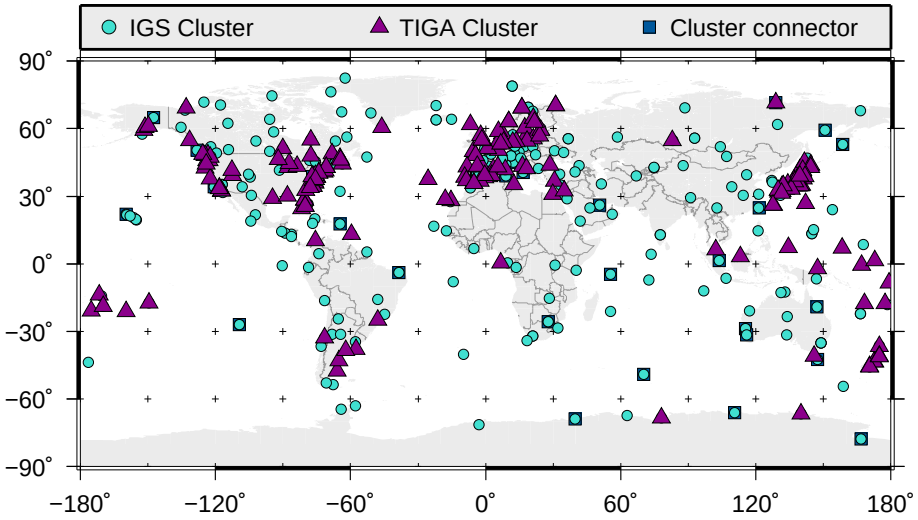

Fig. 1. Global distribution of TIGA and IGS tracking stations used for reprocessing.

SED
4, 1025–1067, 2012

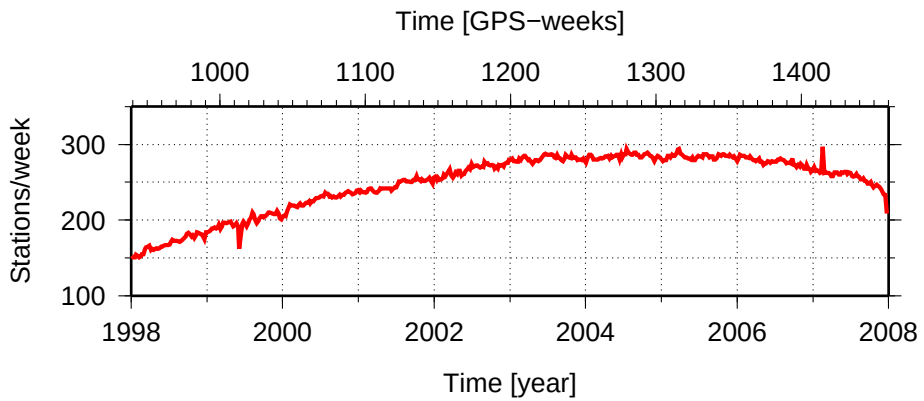

Fig. 2. Number of stations included in weekly GT1 solutions.

SED
4, 1025–1067, 2012

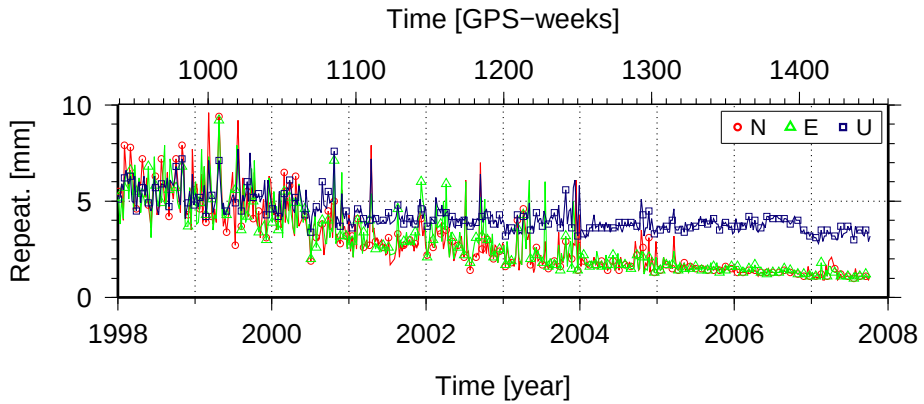

Fig. 3. Weekly overall mean of station coordinate repeatabilites.

SED
4, 1025–1067, 2012

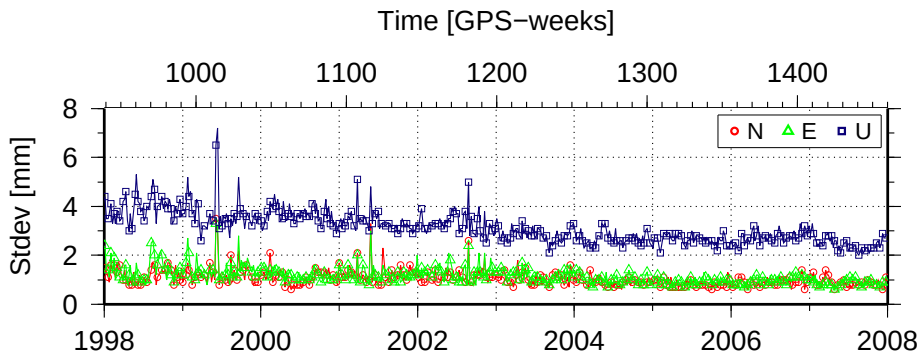

Fig. 4. Standard deviation of solution residuals weighted average with respect to IGS combined solution of repro1 (IG1)

SED
4, 1025–1067, 2012

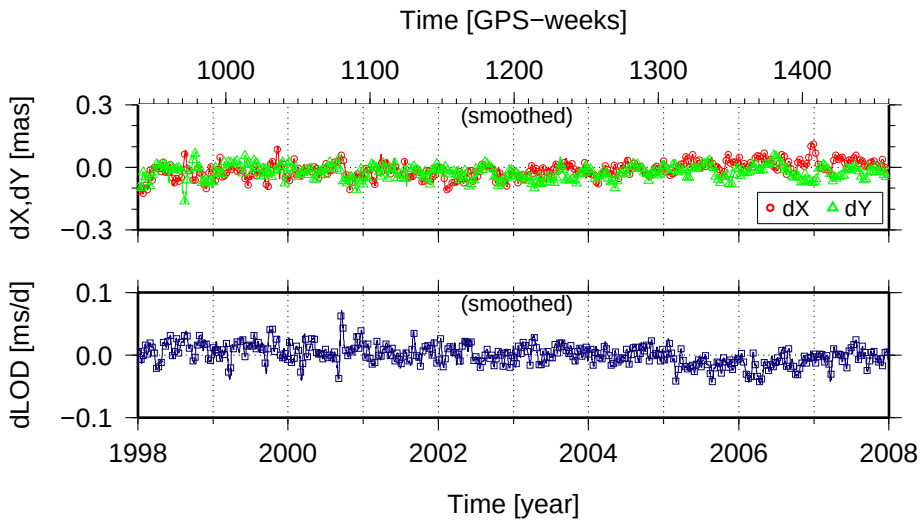

Fig. 5. Comparison of Earth orientation parameters (Pole coordinates X, Y and LOD) of the GT1 solution with respect to IGS combined solution of repro1 (IG1). The plotted values are smoothed with a sliding 3-day mean.

SED
4, 1025–1067, 2012

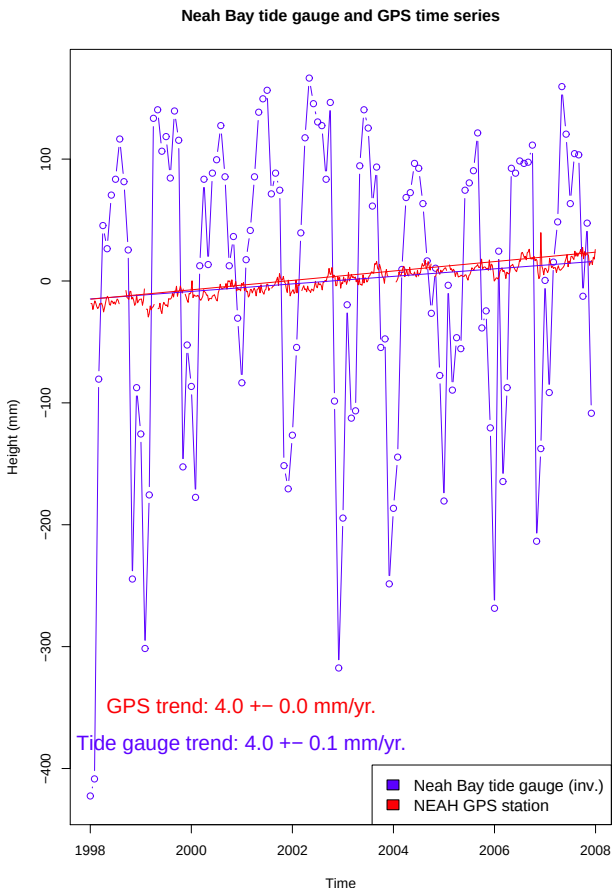

Fig. 6. Both tide gauge and GPS time series show secular height trends of $3.96 \pm 0.02\,\mathrm{mm\,yr^{-1}}$ (GPS) and $4.0 \pm 0.1\,\mathrm{mm\,yr^{-1}}$ (tide gauge).

SED
4, 1025–1067, 2012

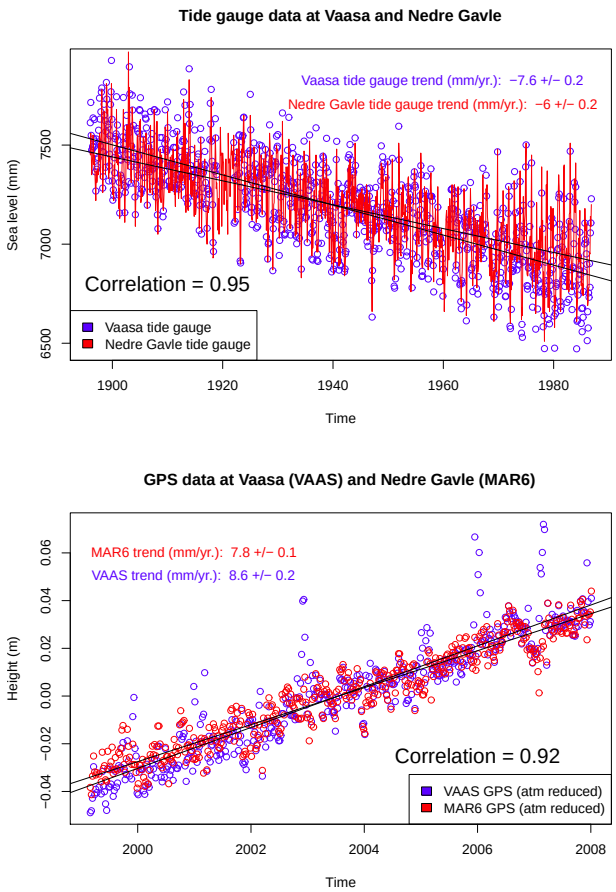

Fig. 7. The upper panel shows the correlation in height trend of two tide gauges Vaasa and Nedre Gavle, located on opposite sides of the Gulf of Bothnia at approximately 340 km distance. The lower panel shows the correlation between their co-located GPS stations, VAAS and MAR6 (with an atmospheric loading correction applied).

SED
4, 1025–1067, 2012

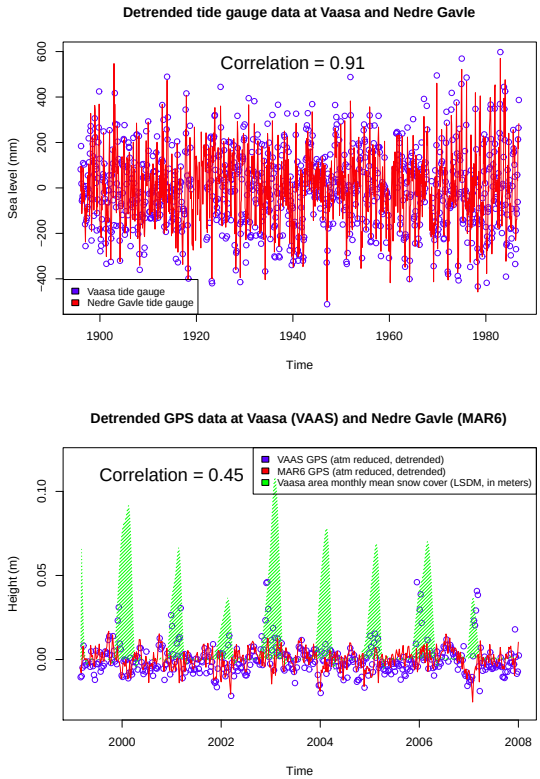

Fig. 8. The upper panel shows the detrended tide gauge time series for Vaasa and Nedre Gavle for the common period (1896–1986). The correlation between the two is very high at $R^2 > 0.9$. The lower panel shows the detrended GPS time series for the co-located stations. The correlation is lowered significantly ($R^2 = 0.45$) by the errors caused through snow cover on the antenna at VAAS station. The green shading depicts the modeled mean snow cover (in meters) at the four neighboring grid points surrounding the station in the LSDM hydrology model.

SED
4, 1025–1067, 2012

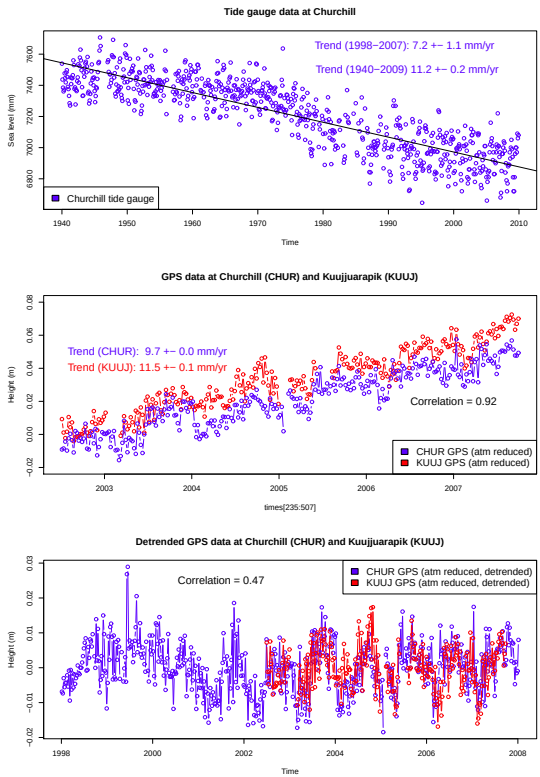

Fig. 9. Data from the tide gauge at Churchill and GPS stations CHUR (Churchill) and KUUJ (Kuujjuarapik), at 1067 km distance. The secular trend in the GPS data is visible nicely in the tide gauge data. Despite their distance, the two GPS stations show significant correlation, also for the detrended series (R = 0.47). The seasonal component of the two stations (not shown) is correlated at R = 0.85. The trend component is obviously correlated most strongly at R = 1.0.

SED
4, 1025–1067, 2012

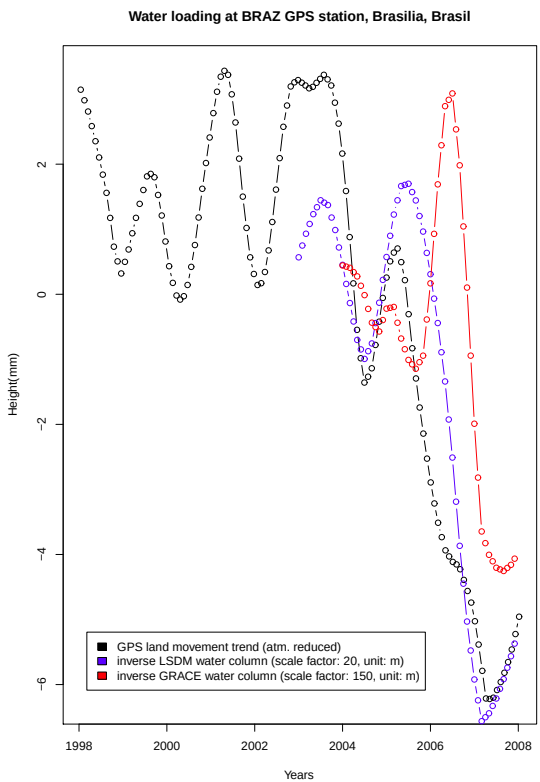

Fig. 10. The picture shows a qualitative comparison of three different signals showing the 2007 drought in Brazil: GPS land movement, (inverse) water storage mass and (inverse) hydrological loading from GRACE. The GPS land movement signal shows a clear negative trend from 2006 on, which can be easily rediscovered in both the LSDM hydrology model and, with a certain lag, the GRACE data. The picture shows the nonlinear trend (seasonal signal and noise removed) for all three time series.

SED
4, 1025–1067, 2012

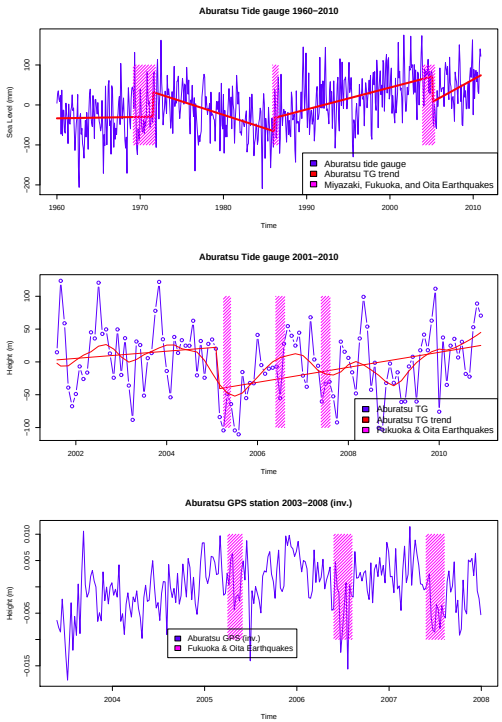

Fig. 11. The picture shows the impact of earthquakes on Aburatsu tide gauge and GPS time series. In the upper panel, trend changes are visible following the 1970 Miyazaki and the 1984 Kagoshima earthquakes, as well as during the Fukuoka earthquakes and aftershocks in 2005. The pink shading marks the interval for possible breakpoints detected by the BFAST algorithm. The middle panel shows a close-up of the tide gauge time series for 2001–2010. Here, a drop in the time series is clearly visible during the 2005 Fukuoka earthquakes (pink shading) and the 2006 and 2007 Oita earthquakes. In the GPS time series shown in the lower panel, a drop in the time series is also visible following the 2005 Fukuoka earthquake, and during the 2006 and 2007 Oita earthquakes.

SED
4, 1025–1067, 2012

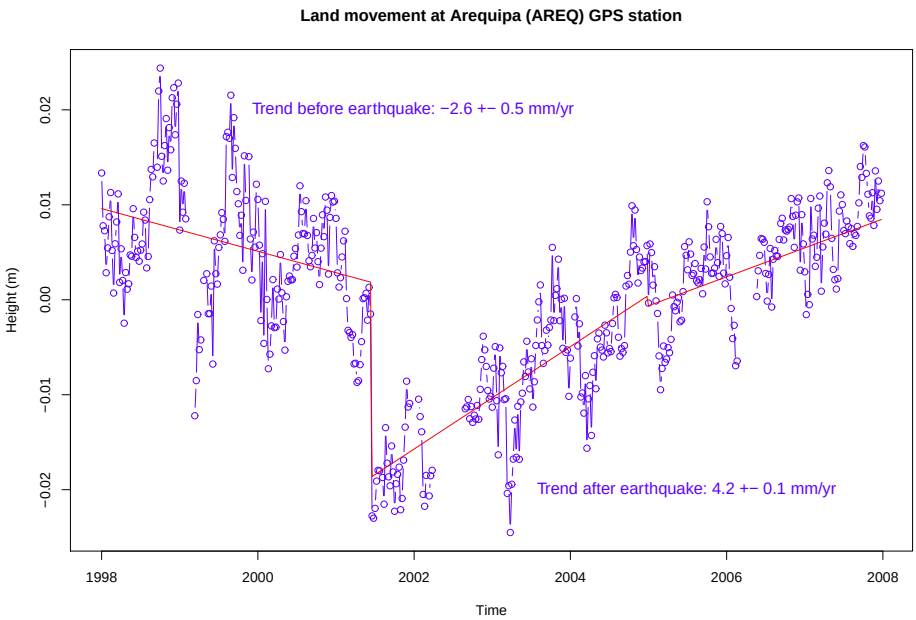

Fig. 12. The picture shows a clear jump in the time series caused by the 2001 Arequipa-Camana-Tacna area earthquake. The trend changes sign from $-2.6 \pm 0.5\,\mathrm{mm\,yr^{-1}}$ to $4.2 \pm 0.1\,\mathrm{mm\,yr^{-1}}$ after the earthquake.

SED
4, 1025–1067, 2012

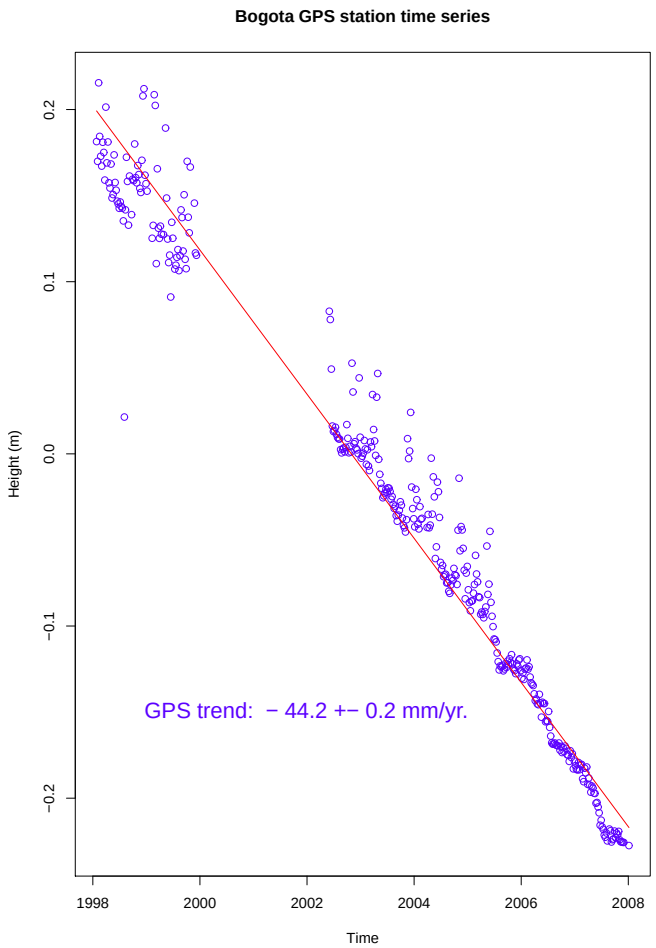

Fig. 13. Subsidence of the IGAC building, on which the GPS station is located, results in a massive secular trend of $-44.2 \pm 0.2\,\mathrm{mm\,yr^{-1}}$ at Bogotà GPS station.

SED
4, 1025–1067, 2012

Reprocessed GPS station height time series

S. Rudenko et al.

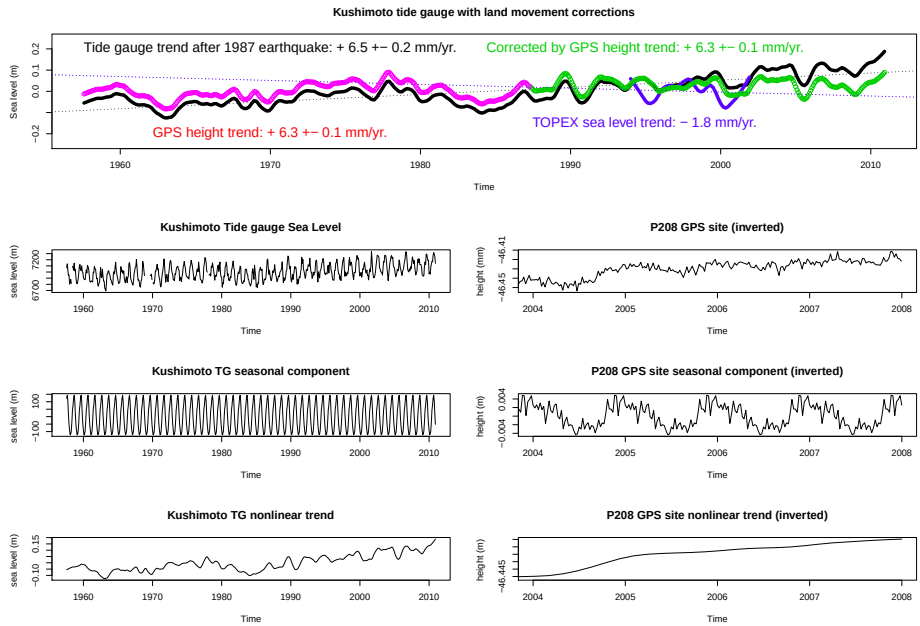

Fig. 14. The apparent sea level rise ($+6.5 \pm 0.3\,\mathrm{mm\,yr^{-1}}$) at Kushimoto tide gauge is most likely caused by land movement following the 1987 Wakayama prefecture earthquake. The GPS station shows a trend of $-6.3 \pm 0.1\,\mathrm{mm\,yr^{-1}}$.

SED
4, 1025–1067, 2012

Reprocessed GPS station height time series

S. Rudenko et al.

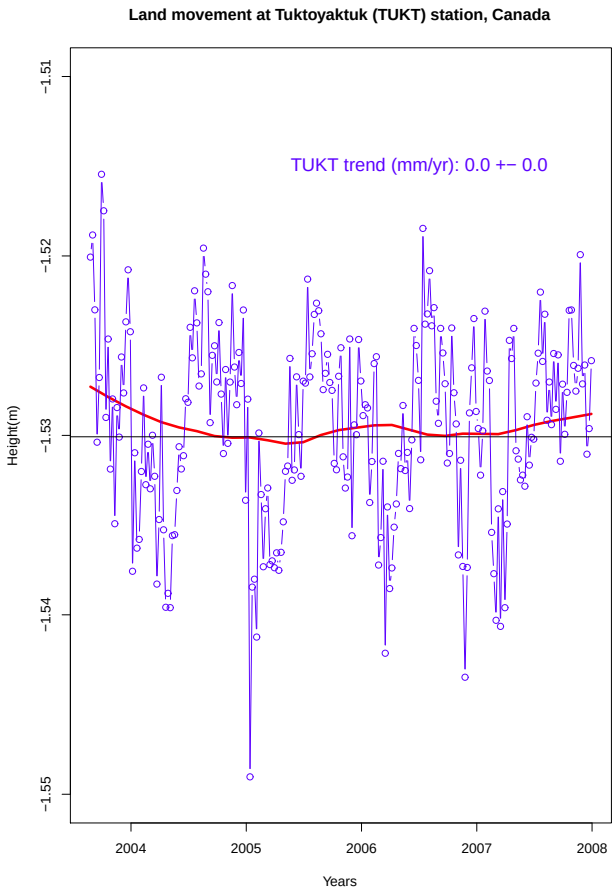

Fig. 15. The Canadian station Tuktoyaktuk shows a zero land movement trend over the last 4.3 yr of the campaign.

SED
4, 1025–1067, 2012